Organic Temperature Sensitive Polyelectrolyte for Core Body Temperature Measurement

Vincenzo Costanza, Dmitriy V. Zhukov, Johnathan Knecht, Nicole J. Higdon, Linghui Wang, Naresh Menon, and Chiara Daraio

***Abstract*— Core body temperature (CBT) is a vital phenotype that provides information on an individual's health and metabolic activity. It correlates with a variety of physical and mental conditions and requires monitoring when an individual is under environmental or medical duress. Current sensing materials lack the desired temperature sensitivity for fabricating ultrathin, wearable CBT sensors with the accuracy needed for medical applications. Here, the realization of an ultrathin CBT sensor based on dual heat flux (DHF) thermometry is reported, uniquely enabled by the application of a novel class of synthetic polymers. By optimizing the chemical composition, the material's properties were tuned to achieve an optimal temperature response. Furthermore, the measurement error in the device was evaluated using Finite Element analysis. Building on this knowledge, this highly temperature-sensitive polymer was embedded into an ultrathin DHF sensor, and its sensitivity and repeatability were characterized using an anthropomorphic phantom model. The results presented in this work pave the way for first-in-class wearable and accurate DHF sensors, allowing continuous CBT monitoring.**

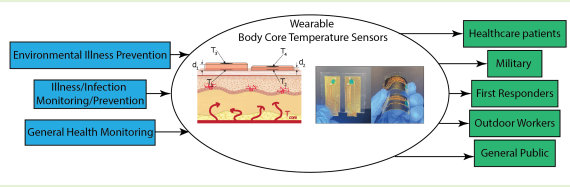

***Index Terms*— bioinspired material, temperature measurement, temperature sensor, wearable health monitoring, wearable sensor.**

I. Introduction

IN all mammals, core body temperature (CBT) is a highly conserved phenotype that is an accurate indicator of systemic metabolic activity and its regulation. Monitoring CBT in clinical settings has been shown to impact surgical outcomes [1]–[4], and is a leading indicator of immune system response from inflammation and infection [5]–[9]. Furthermore, in everyday scenarios CBT has been linked to general wellbeing as it can be used to quantify calories burnt over time [10], [11], onset of ovulation cycles [12], the circadian cycle and sleep quality [13], [14], mental health [15], and degenerative diseases such as Alzheimer's and Parkinson's [16], [17]. Continuously recording CBT can therefore be extremely beneficial for a wide spectrum of applications, spanning from hospital care to the monitoring of indoor and outdoor activity. However, the CBT cannot be easily measured to the required degree of accuracy. The gold standard for the measurement of CBT is the pulmonary artery catheter, which records the temperature of the blood flowing directly from the heart [18]. This method is highly invasive and is used only in specific surgeries. Other methods rely on the measurement of rectal temperature [19] or the ingestion of radio pills [20]. However, these methods are invasive and not suitable for continuous monitoring. At the same time, there are several methods to measure peripheral body temperature by placing thermometers or standoff IR scanners on the skin that are both continuous and non-invasive. However, peripheral body temperature is poorly correlated with core body temperature. In fact, thermoregulatory processes regulate the core body temperature, while the temperature at the surface and peripheries of the body are affected by various extraneous factors such as placement of the thermometer, ambient temperature, and perfusion that do not reliably correlate with the underlying metabolic function. As such, peripheral measurements tend to be inaccurate to predict CBT. To overcome these limitations, some strategies that employ the measurement of heat flux have been used. Dual-heat flux (DHF) thermometry measures the flow of heat (flux) that flows out of the body along two different thermal paths, to decouple the system from the thermal resistance of the underlying tissue [21]–[25]. DHF sensors have demonstrated effective monitoring of CBT in patients both at rest and during exercise [26]. However, DHF sensors are typically bulky and thick (up to 15 mm), the thinnest proposed device the authors have found measures 5.44 mm [27]. Furthermore, the limiting factor in current DHF sensors is the accuracy of the individual temperature sensing

This work was in part performed under U.S. Army contract # W5170123C0086.

V. C. was with the Division of Engineering and Applied Sciences, California Institute of Technology, Pasadena, CA 91125. He is now with Hardware Technology Apple Inc, San Diego, CA 92122 USA

L. W. was with the Division of Engineering and Applied Sciences, California Institute of Technology, Pasadena, CA 91125. She is now with Research and Development at Bayer, Chesterfield, MO 63017 USA

D. Z. , J. K., N. M. are with Chromologic LLC, Monrovia, CA 91016

N. H. and C. D. are with the Division of Engineering and Applied Sciences, California Institute of Technology, Pasadena, CA 91125. (e-mail: daraio@caltech.edu).

elements [28]. In this work, we employ a novel temperature responsive polymer that demonstrates record temperature sensitivity orders of magnitude higher than vanadium oxide and other cutting-edge temperature sensing materials. [29], to create ultra-thin and wearable DHF thermometers for CBT. We designed the sensors' geometry to optimize for tissue depth sensitivity, and evaluated its errors using Finite Element (FE) analysis. Furthermore, we characterized and improved the chemical composition of the temperature responsive polymer, to obtain higher temperature sensitivity. For data acquisition, we designed and fabricated a custom electronic board that achieved a readout accuracy of 4 mK. Finally, we fabricated an integrated prototype that was tested with an anthropomorphic phantom model demonstrating the ability to read CBT with an accuracy of ± 0.25 °C.

II. Results

A. DHF Calorimetry for Measuring CBT

In general, measurements of skin temperature do not correlate well with CBT since thermoregulatory processes keep peripheral areas at lower temperature than the core. Nevertheless, under certain conditions, skin temperature can reflect with high precision the core temperature. For example, in the absence of heat flow, skin temperature equals the temperature of the inner tissues (deep core temperature): Zero-heat-flux (ZHF) thermometers are based on this principle. In ZHF thermometers a heat source is used to counterbalance the heat flowing out of the body to generate a zero-heat flow region on the skin. A pair of temperature sensors separated by a thermal insulator measures the heat flow and provide feedback to the heat source. Once isothermy is achieved, the bottom sensor measures the skin temperature which corresponds to the CBT. ZHF thermometers, however, require a constant power source for the heater and due to the inaccuracy of the temperature sensor they need a rather thick insulating layer. All these factors render ZHF thermometers unsuitable for wearable applications. To avoid the need of a heater to generate zero heat flux, dual heat flux (DHF) thermometers were developed [21]. In this device, a heat flux sensor consists of a pair of temperature sensors separated by an insulator. The DHF thermometer pairs two heat flux sensors, with different insulator thicknesses, placed next to each other. By knowing the thermal resistance of the insulator dividing the temperature sensors, it is possible to rule out the thermal resistance of the tissues beneath the skin. As shown in Fig. 1(a), the CBT T_B is then calculated from the temperatures of the four sensors T_1, T_2, T_3, T_4 as [21]:

$$T_B = T_1 + \frac{(T_1 - T_2)(T_1 - T_3)}{K(T_2 - T_4) - (T_1 - T_3)}, \tag{1}$$

Where K is the ratio between the thermal resistance paths under the two heat flux sensors and must first be calibrated. K can be calculated using (1) and empirical measurements as [21]:

$$K = \frac{(T_B - T_2)(T_1 - T_3)}{(T_B - T_2)(T_2 - T_4)} \tag{2}$$

The thermal resistances of the two different paths determine the temperature difference between the bottom and the top surfaces. Therefore, the thickness of the insulating layers needs to allow the development of a thermal gradient that is measurable by the temperature sensors placed at the top and bottom of each heat flux sensor. To decrease the thickness of the heat flux sensors, extremely temperature sensitive materials, with high accuracy, must be used. It has been recently reported how a particular class of polyelectrolytes shows significantly high temperature sensitivity [29]–[32]. These synthetic polymers are characterized by carboxyl and hydroxyl groups placed along the backbone, which interact with metal cations (e.g., Ca^{2+}, Co^{2+}, Cu^{2+}) present in the polymer matrix. The temperature variation modifies the thermal energy of the system resulting in cations to proportionally hop from one coordination site to another, leading to a change in the conductivity. In this work, we synthesized 2-hydroxyethyl acrylate acrylic acid (HEA-AA) [29] with a combination of metal cations to be used for the fabrication of the DHF sensor. The polymer was deposited on two thin polyimide (PI) layers. To generate two different thermal paths, the PI substrates had different thicknesses of 260 and 100 µm, respectively. On the surfaces of the PI layers, prepatterned Cu/Au plated electrodes were used to electrically connect the HEA-AA to measure the change in conductivity. Two 10 µm thin HEA-AA layers were deposited on the electrodes and then insulated with 50 µm thick PET layers (Fig. 1(b)(Top)) from external agents (e.g., room humidity). The resulting DHF sensor is less than 500 µm thick and highly flexible. This flexibility is a direct result of the ultrathin nature of these sensors and enables the resulting sensors to be conformally applied to the curvature of the body(Fig. 1(b) (Bottom)).

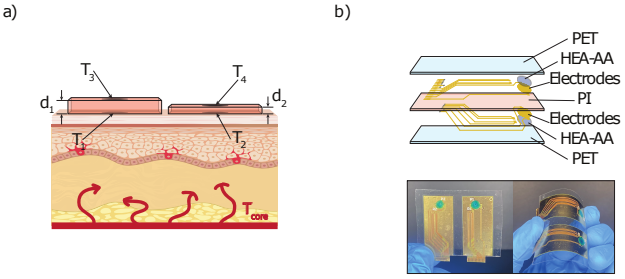

Fig. 1. **Dual Heat Flux sensor and HEA-AA integration.** (a) Dual Heat Flux working principle. (b) Fabricated DHF sensor. Top: schematic of the sensor integrating HEA-AA in the architecture. Bottom: picture of the DHF sensor using Co^{2+} ions, flat (left) and bent (right).

B. Temperature Response Characterization

From a device perspective, the HEA-AA polymer can be approximated to act as a temperature-dependent resistor since the polymer's conductivity varies as a function of temperature. However, the relationship between the temperature

and resistance for this class of polymers is nonlinear and cannot be represented by a constant temperature coefficient of resistance [29]–[32]. The polymer's conductivity-temperature dependence needs to be generalized to a temperature dependence of the complex admittance Y (or impedance Z). In addition, to avoid charge accumulation in the devices, the change of the polymer response as a function of temperature needs to be characterized by an AC current. Previous work has characterized HEA-AA crosslinked with divalent calcium at specific frequencies, or in a narrow frequency range [29]. As a reference, Fig. 2(a) shows the absolute value of the admittance as a function of frequency (1 Hz to 100 kHz) measured at 35 and 45°C and at a constant relative humidity (RH) of 10 %. In the medium frequency region, a strong frequency dependence does not appear, while at low and high frequencies the spectrum presents two strong dispersive regimes. This behavior is in line with the behavior of other ionic conductors, where polarization and dielectric relaxations arise in these frequency regions [33], [34]. The phase of the admittance (i.e., the phase difference between the applied voltage and the resulting current) also shows a strong dependence on temperature as well as on the applied frequency (Fig. 2(b)). Therefore, we can define the material's temperature response $R^*(\omega)$ as the ratio between the admittance $Y^*(\omega, T)$ at highest temperature T_{max} divided by the admittance measured at the lowest temperature T_{min}, for a specified temperature range:

$$R^*(\omega) = \frac{Y^*(\omega, T_{max})}{Y^*(\omega, T_{min})} \tag{3}$$

As a result, the absolute value of the response $|R^*(j\omega)|$ corresponds to the ratio of the absolute value of the admittance $|Y_0(\omega, T)|$, while the phase of the response $R^*(j\omega)$ corresponds to the difference between the phase of admittance $\theta(\omega, T)$:

$$\begin{aligned} |R^*(\omega)| &= \frac{|Y_0(\omega, T_{max})|}{|Y_0(\omega, T_{min})|} \\ R^*(j\omega) &= |\theta(\omega, T_{max}) - \theta(\omega, T_{min})| \end{aligned} \tag{4}$$

To maximize the temperature sensitivity, we prepared different HEA-AA samples crosslinked with Ca^{2+}, Co^{2+}, Cu^{2+}, Mg^{2+}, Zn^{2+}. Each of these ions has a different binding energy with the polymer backbone that results in a different temperature response. The temperature response is directly correlated to the activation/binding energy E_a of the metal ion with the acid and polar groups along the polymer backbone. This concept becomes clearer in the Arrhenius representation, when considering the ion bulk conductivity $\sigma_0(T)$, the temperature response is proportional to the activation energy for ion hopping:

$$\begin{aligned} E_a &= \frac{log(\sigma_0(T_{max})) - log(\sigma_0(T_{min}))}{1/T_{max} - 1/T_{min}} \\ &= \frac{log\frac{\sigma_0(T_{max})}{\sigma_0(T_{min})}}{1/T_{max} - 1/T_{min}} = \frac{logR_0}{1/T_{max} - 1/T_{min}} \end{aligned} \tag{5}$$

where $R_0 = \sigma_0(T_{max})/\sigma_0(T_{min})$ is the conductivity DC response. Our previous work has shown how increasing the number of carboxyl and hydroxyl groups increases the polymer's temperature response [29]. This behavior is a direct consequence of the strength of the interaction between the polymer backbone and the metal ion: a higher number of functional groups, creating a coordination complex with higher binding/activation energy E_a. A stronger interaction between the polymer complex and the metal cation could also be achieved by choosing an ion whose affinity to the coordination complex is particularly high. Previous studies suggest that the geometry of the electronic orbitals combined with the spatial arrangement of the coordination complex will result in larger activation energies [35]–[37]. Therefore, we compared different polymer-metal cation combinations (i.e., Ca^{2+}, Co^{2+}, Mg^{2+}, Cu^{2+}, and Zn^{2+}) to determine the one that has the highest temperature response. Fig. 2(c) and 2(d) show the absolute value and phase response spectra for the different cations in the temperature range 35 to 45 °C. Co^{2+} shows the highest temperature response both in terms of absolute and phase response. As previously reported [32], an optimal water content is needed to measure a high temperature response. Water can modify the ion's transport activation energy in multiple ways, for example by varying the coordination environment of the ions, as well as the polymer's segmental motion. Water molecules can also provide additional charge carriers (protons) with a lower activation energy, which can lower the temperature response. To minimize the effect of the water concentration within the polymer, we performed all characterization at constant humidity (RH 10%). However, every ion has a different water affinity (Ca^{2+} is highly hygroscopic, while Co^{2+} and Cu^{2+} have lower water affinity). To evaluate the difference in water content between the various ions, we measured the conductance at constant temperature (35 °C) (Fig. 2(e)). Among the different ions, Co^{2+} has the lowest current, suggesting that the water content is within the optimal concentration to register an optimal temperature response. Based on this analysis, HEA-AA crosslinked with Co^{2+} ions was selected as the ideal material to fabricate a DHF calorimeter.

Fig. 3(a) shows the typical calibration curve for the selected material. The absolute value of the current increases from 300 pA to 2.2 nA, while the current phase difference decreases from 55 to 20 degrees over a 10 °C temperature change. The current's phase difference varies linearly with temperature, and the current's absolute value relationship to temperature is exponential. For optimal performance, we can mix and match the calibration methods of the four sensors, empirically determining the better one (phase vs. current) during character-

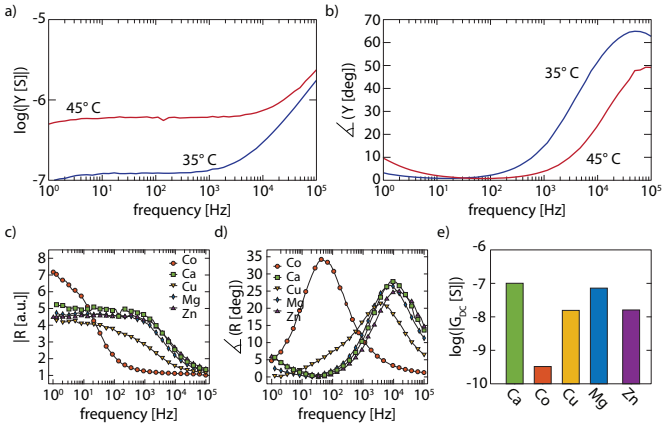

Fig. 2. **HEA-AA characterization.** (a) Typical absolute value of the conductance spectra for a sample crosslinked with Ca^{2+} and measured at RH 10%. Blue line absolute value measured at 35 ℃, red line absolute value measured at 45 ℃. (b) Typical phase of the conductance spectra for a sample crosslinked with Ca^{2+} and measured at RH 10%. Blue line phase measured at 35 ℃, red line phase measured at 45 ℃. (c) Absolute value of the response as a function of frequency for samples crosslinked with different ions measured at RH 10%: orange dots Co^{2+}, green squares Ca^{2+}, yellow down triangles Cu^{2+}, blue diamonds Mg^{2+}, purple triangles Zn^{2+}. The markers represent a subset of the actual data set. (d) Phase of the response as a function of frequency for samples crosslinked with different ions measured at RH 10%: orange dots Co^{2+}, green squares Ca^{2+}, yellow down triangles Cu^{2+}, blue diamonds Mg^{2+}, purple triangles Zn^{2+}. The markers represent a subset of the actual data set. (e) DC conductance of the samples crosslinked with different ions at 35 ℃ measured at RH 10%.

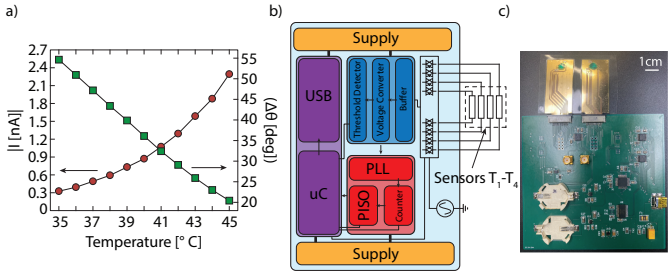

Fig. 3. **Sensors calibration and readout.** (a) Sensor temperature calibration. Red circles current absolute value, green squares current phase. (b) Schematic of the readout system. (c) Picture of the readout system and the DHF sensor.

ization. A custom readout system was designed to accurately sample the current and phase response (Fig. 3(b) and 3(c)). A sine wave oscillator generates the harmonic voltage to be applied to the sensor through an analog multiplexer. The resulting current flowing through each individual sensor is then converted to a voltage and then amplified by means of an instrumentation amplifier. The applied voltage and the measured current were then converted to square waves. Because of the reactance of the polymer, the voltage and current have a phase difference. This phase difference is measured by a phase detector, which generates a pulse that corresponds to the time delay between the two signals. The pulse width is then quantified through a 2 MHz 16-bit counter. Given the frequency of the applied voltage $f_{excitation}$, the frequency of the counter clock $f_{counter}$, the phase difference $\Delta\Theta$ correlates to the counter counts n_{count} through the relation:

$$\Delta\Theta = \frac{n_{count}}{f_{counter}} \cdot 360° \cdot f_{excitation} \tag{6}$$

By measuring the phase response, not only the sensor's output is linearized with respect to temperature, but also considerably higher accuracy can be achieved without the need for a specific analog to digital converter (ADC) architecture. With the implemented circuit, a minimum phase shift of 0.006° can be measured, which corresponds to a resolution of approximately 4 mK.

C. Error Analysis

The optimization of HEA-AA composition ensures that the temperature response of the polymer has the proper sensitivity to measure the small temperature differences across the DHF sensor. However, the precision of the temperature sensors is not the only factor that contributes to the DHF sensor's accuracy. More specifically, in the derivation of(1) some assumptions were made to reach a simple analytical solution. In particular, the heat flux was assumed to be totally transversal with no longitudinal component. We will show that this assumption is the major contribution to the theoretical error of the DHF architecture. Fig. 4(a) Top) shows the transversal and longitudinal thermal gradient that is established in the chosen geometry calculated from the FE simulation. The transversal thermal gradient develops from the bottom of the tissue layer and it is funneled towards the heat flux sensors. At this interface, two different thermal gradients appear because the heat flux sensors have different thicknesses. Because we chose to use very thin insulating layers for our sensors (260 and 100 µm, respectively), the temperature difference between the top and the bottom of the sensors is in the order of 50 mK. However, as it can be seen in Fig. 4(a) (Bottom) there is a non-zero longitudinal temperature gradient that develops over the xy plane. The generation of a transversal thermal gradient has to be attributed to the non-uniform heat exchange along the surface boundaries on the xy plane. Previous works studied the system using radiation or convection boundary conditions without taking into account how they affected the measurement error. [23], [38] In order to analyze how the different heat exchange phenomena affect the measurement, we characterized the error e for the two different conditions and we correlated it with the temperature gradient ∇T between the temperature at the center of the top surface of one of the two heat flux, T_A, and the one at the corner on the same surface, T_B. By doing so, we can correlate the amount of transversal thermal gradient to the measurement error. First, we analyzed the heat exchange at the boundaries through radiation only (Fig. 4(b)). The rate of heat exchange through radiation $-\boldsymbol{n} \cdot \boldsymbol{q}_0$ at a surface temperature T depends on the surface emissivity ϵ and the ambient temperature T_{amb}, according to the Stefan-Boltzmann law:

$$-\boldsymbol{n} \cdot \boldsymbol{q}_0 = \epsilon\sigma(T_{amb}^4 - T^4) \tag{7}$$

where σ is the Stefan-Boltzmann constant. As T_{amb} increases, there will be a lower surface to ambient radiation which will create a smaller gradient on the xy plane. Fig. 4(b) indicates that the decrease in the thermal gradient proportionally leads to a smaller error. Similarly to radiation, convective heat exchange q_0 is determined by ambient temperature T_{amb} and the heat transfer coefficient h:

$$q_0 = h(T_{amb} - T) \tag{8}$$

For convective heat exchange with the ambient, the heat transfer coefficient depends on several factors, among which relative humidity or air flow speed. However, the heat transfer coefficient in normal conditions ranges between 0.1 – 10 W/m^{2}K. For this simulation, we only modified the heat transfer coefficient keeping the ambient temperature constant. Fig. 4(c) shows the error as a function of h: for values below 1 W/m^{2}K the error remains low, however it drastically increases above this threshold. This behavior correlates closely with the development of a larger thermal gradient as the heat transfer coefficient increases: for $h < 1W/m^2K$ the transversal gradient remains low, while above this value it starts to increase. It is therefore clear how the measurement error is caused by the thermal gradient on the xy plane, whose magnitude is set by the heat exchange characteristics at the boundaries. When combining both heat exchange physics, the complete measurement error can be further analyzed (Fig. 4(d)). When radiation is combined with convection, the effect of convection does not drastically impact the error as long as the heat transfer coefficient is kept low. For higher h (e.g., above 1 W/m^{2}K), the convective heat exchange dominates, leading to a larger error. The analysis of the theoretical error indicates that in order to reduce the measurement error in the experimental setting, both the radiation and convection need to be reduced to achieve accurate results. Radiation heat exchange is inevitable and can only be limited by lowering the emissivity of the substrates, which is constrained by the choice of the available materials used to fabricate flexible substrates. Convection can be drastically lowered by the use of materials to thermally insulate the sensor. This approach would lead to bulkier and less flexible sensors. However, as previously shown, it is sufficient to ensure that the heat transfer coefficient is below 1 W/m^{2}K in order to minimize the effect of convection. This is the case for most everyday conditions under normal clothing. [39] The extensive use of thermal insulation on the device is not required and a clothing layer will be used to reduce to the minimum convective heat. Moreover, it has been shown that the error given by the transversal gradient can be minimized by modifying (1) to: [23]

$$T_B = T_1 + \frac{(T_1 - T_2)(T_1 - T_3)}{K(T_2 - T_4) - (T_1 - T_2)} \tag{9}$$

Using (9) and considering both radiative and convective heat exchange (fixed to 1 W/m^{2}K), it is possible to calculate the penetration depth as a function of the ambient temperature (Fig. 4(e)). The maximum penetration depth that this method can achieve is the maximum tissue thickness which allows the calculation of the CBT with an error below 0.25 °C. This error threshold was chosen to be well within the clinically acceptable limits of bias, as defined by previous studies [40]–[44]. The penetration depth varies from 6.4 mm at 20 °C to almost 10 mm at 30 °C. This analysis allows us to clarify the theoretical limitations of the DHF 1D model given the parameters of our device.

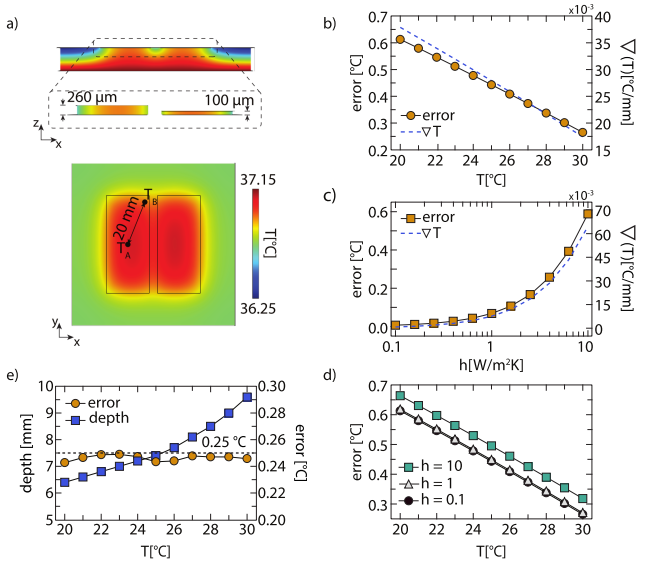

Fig. 4. **FEM Analysis on the DHF architecture.** (a) Thermal gradient developed across the xz (Top) and xy (Bottom) planes. (b) Error (orange circles) and temperature gradient (blue dashed line) calculated as a function of external temperature for radiative heat transfer. (c) Error (orange squares) and temperature gradient (blue dashed line) calculated as a function of heat transfer coefficient for convective heat transfer. (d) Error calculated as a function of external temperature for both radiative and convective heat exchange at different heat transfer coefficients: teal squares h = 10 W/m^{2}K, gray triangles h = 1 W/m^{2}K, black circles h = 0.1 W/m^{2}K. (e) Penetration depth (blue squares) and corresponding error (orange circles) as a function of external temperature at constant heat transfer coefficient h = 1 W/m^{2}K.

D. CBT Measurement

Combining the results of the ion comparison in HEA-AA with the readout system and the information gathered by the theoretical error analysis, HEA-AA temperature sensors were successfully integrated in the designed DHF architecture. The individual temperature sensors were characterized between 35 °C and 45 °C to obtain the temperature calibration curve. The phase-temperature calibration data was then fit to a first-degree polynomial and the two fit parameters were used to convert the acquired phase to temperature values (Fig. 5(a)). The linear fit diverges for higher temperature, but it gives an optimal representation for T < 43°C, with coefficient of determination R greater than 0.9989. To simulate the CBT measurement, we built a custom-made setup, where both the accuracy and the time response of the sensor can be estimated (Fig. 5(b)). A water bath was used to achieve a constant temperature T_{set} of 37 °C, while a thin copper layer immersed in the bath was used to obtain a homogeneous temperature across the

surface. To simulate the skin, we used a rubber mat with a thermal resistance similar to that of human tissue. To evaluate the sensor's performance for different skin thicknesses, rubber mats of 2, 4, 6, and 8 mm thick were used. The DHF sensor was connected to the readout board, which in turn was connected to a computer. At the same time, an IR camera measured the temperatures of the water bath and the copper layer to ensure that the correct temperature was established in the bath. A piece of regular clothing (few millimeters thick cotton shirt) was used to reduce the heat transfer coefficient with the ambient air. We first determined the ratio between the thermal resistance paths K using (2) with data obtained from the 2 mm thick rubber mat. Then, the T_{set} was computed from the individual temperatures using (9). Fig. 5(c) shows the estimated CBT using the DHF sensors for the different mat thicknesses. The green area in the plots indicates the ± 0.25 °C maximum allowed error. When the DHF sensor is not thermally insulated with clothing, the estimated T_{set} has an error greater than 0.25 °C for mats thicker than 2 mm, with a maximum error of 0.76 °C for the 8 mm thick mat. When the DHF thermometer is covered with clothing, the sensor's performance greatly improves. Error within the 0.25 °C bounds was measured for a mat thickness of 6 mm, while for an 8 mm thick mat the maximum error was 0.33 °C. These results are in line with the theoretical calculation presented in the previous section. The transversal heat flux is the main source responsible for the error in the DHF architecture. Reducing the heat transfer between the boundaries and the ambient air results in lower thermal gradient across the sensor, which corresponds to a higher sensor accuracy. When covered with a piece of clothing, the heat transfer coefficient of the convective transfer between the sensor and the ambient is reduced, resulting in a smaller error. Lastly, we analyzed the transient behavior of the DHF thermometer. We increased the temperature of the thermal bath from 37 to 39 °C and estimated T_{set} using the 6 mm mat while the sensor was covered with a piece of clothing. Fig. 5(d) shows the time evolution of the reconstructed temperature when this step change was made. We calculated the response time as the time the system needed to recover to an error below 0.25 °C. For the selected mat thickness, the reconstructed temperature fell within the accepted error approximately after 15 minutes.

Once we established the response time of our DHF setup, we investigated its CBT resolution on a human phantom model (Fig. 6). A thermocycler (Bio-Rad C1000) was used for precise temperature control and its temperature setting was considered ground truth CBT (Fig. 6(a)). We used a 5 mm thick 7% Agar gel to simulate human subcutaneous tissues as previously described, [45]. The gel was sealed with *Saran* wrap to prevent water evaporation, with entire assembly covered with a Petri dish to prevent fluctuations due to ambient convection (Fig. 6(b)). The DHF sensor was connected to the impedance analyzer (Zurich Instruments, MFIA 5 MHz) through our custom interface PCB, and both the phase and the absolute value of current calibrations were considered in selection of the optimal response to temperature for each of the polymer sensors. By using phase response calibrations for sensors T1 and T2, and current amplitude calibration curves for T3 and

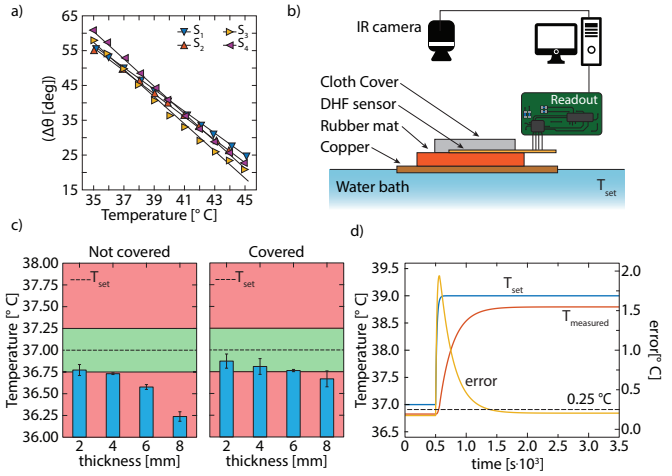

Fig. 5. **CBT measurement.** (a) Phase calibration curves for the different temperature ulsensors in the range 35 and 45 °C. (b) Setup to measure the CBT. The core temperature is simulated by a water bath set to the desired value T_{set}. A thin copper layer is used to achieve homogeneous temperature over the analyzed surface. A rubber mat simulates the tissue layer between the core and the sensor. The DHF sensor is placed on top of the rubber mat and then covered by a piece of clothing. (c) Calculated CBT for a set temperature of $T_{set} = 37°C$, for different thicknesses of the rubber mat (2, 4, 6, and 8 mm, respectively). Measured CBT when the sensor is exposed to convective heat exchange (left) and when a piece of clothing is applied to insulate the sensor from the environment (right). (d) Step response for the DHF sensor calculated with the 6 mm rubber mat when T_{set} is increased from 37 to 39 °C. Blue line represents thermal bath temperature, orange line represents the DHF sensor output temperature, the yellow line represents the absolute error in the measurement.

T4, we obtained the best fit between our CBT estimation and the ground truth in the region spanning hypothermic and hyperthermic temperatures (25-45 °C) (Fig. 6(c)).

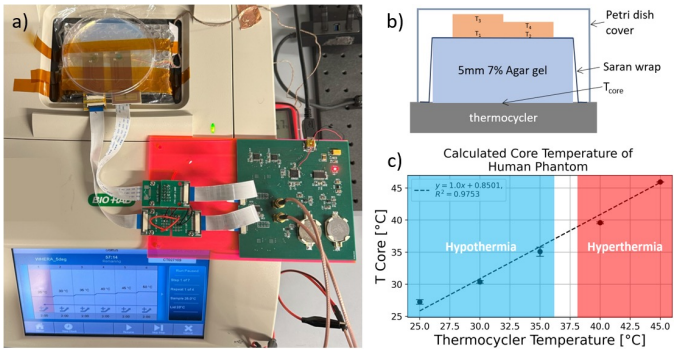

Fig. 6. **DHF sensor's CBT resolution.** (a) Photo of human phantom experimental setup. The pixels are plugged into the breadboard PCB, which is interfaced with the impedance analyzer (not shown). (b) Schematic of the experimental setup for human phantom model. (c) Calculated CBT for various $T_{set} = 25°C, 30°C, 35°C, 40°C, 45°C$, representing hypo and hyperthermia for the human body (identified in blue and red respectively).

III. Conclusions

In this work, we showed the fabrication of a CBT sensor, integrating a thermally responsive polymer into the DHF thermometer architecture. We optimized the polymer's composition by choosing the best metal cation that showed the

highest response. Co^{2+} was found to be the best cross-linking ion because it was linked to an optimal water content. We employed the complex temperature sensitivity to design a readout system, in which the temperature could be related to both the current response and the phase of the sensor's admittance, achieving a sensitivity of 3.5 °/°C and a resolution of ± 4 mC. By simulating the DHF architecture, we found a correlation between the theoretical error and the longitudinal thermal gradients that develop over the sensors. Furthermore, we analyzed the influence of different boundary conditions on the device performance and calculated the corresponding errors and penetration depth. We fabricated a DHF thermometer employing the optimal polymer's composition and used a custom-built readout system to measure CBT on a phantom setup. We showed that, as described by the FE simulations, the measurement error can be reduced by lowering the heat exchange at the boundaries. The fabricated sensor has an error below ± 0.25 °C for a thickness up to 6 mm and a time response of 15 minutes.

IV. Experimental Section

A. Polymer Synthesis

Polymer synthesis was carried out similarly to prior work [29]. Polymer synthesis details can be found in the supplementary information.

B. FEM Analysis

The geometry was simulated using COMSOL Multiphysics. For simplicity, the skin was simulated as homogeneous medium and the bioheat generation or blood perfusion were not taken into account. The substrate was implemented using the thin layer module to decrease computation time and achieve a better result. A general layer type was considered to take into account both the normal and tangential heat fluxes. Three different situations were considered for the boundary conditions: radiation heat exchange, convection heat exchange, and mixed radiation and convection heat exchange. We first calculated the heat transfer in the system tissue/sensor. Then, we used the output of this simulation to compute the heat exchange at the boundaries through radiation and convection. The error was calculated as the difference between the temperature set at the bottom boundary of the tissue and the temperature calculated with (1). The temperature gradient was estimated as the difference between the temperature at the center on the top surface of the thicker heat flux sensor and the temperature 20 mm away along the diagonal on the same surface (Fig. 4(a)). The maximum penetration depth was calculated as the thickness at which the error was below 0.25 °C. The thickness of the tissue was incremented by 100 µm.

C. Electrical Readout Circuitry

Details on the design and characterization of the readout circuit can be found in the supplementary information.

D. Thermal Response and Calibration

Details on the thermal response testing and instrument calibration can be found in the supplementary information.

E. CBT Measurement at Various Depths

Polyimide substrates with double sided prepatterned copper/immersion gold electrodes (35 µm and 3 µm, respectively) were purchased from PCBWay. On these substrates 5 µL of HEA-AA crosslinked with various ions was deposited and dried overnight under vacuum. The sensors were then insulated with a 50 µm PET layer to shield the polymer from humidity. Pt100 thermometers were placed on each of the four polymer sensors to obtain the calibration curves (Fig. 5(a)). Next, the assembled DHF thermometer was ready for CBT measurement. Rubber mats of different thicknesses were used to simulate human skin and subcutaneous tissue (Fig. 5(b)). To further reduce the effect of convective heat exchange with the environment, the DHF sensor was further covered with a piece of cloth. The experiment was performed at room temperature. The rubber mat along with the DHF sensor was placed on a thermal bath (Thermo Scientific Precision GP 05) to create a stable temperature, which simulated the core temperature, and kept at 37 °C (Fig. 5(c)). Data from individual sensors were acquired through the previously described readout system at a sampling rate of 21.5 Hz. To measure the response time, we increased the bath temperature from 37 to 39 °C and analyzed the time evolution of the sensor's output when placed on the 6 mm mat (Fig. 5(d)). To replicate the human skin, 7% Agar gel was used, since it matches the thermal properties of human tissue well [46]. An Agar gel layer of 5 mm thickness was used. A PCR thermocycler is used for accurate temperature control, and the temperature at the interface between Agar layer and thermocycler is verified using a thermistor. The agar gel was sealed using Saran wrap to prevent water evaporation. The pixels were pressed down to the Agar phantom layer using polyimide tape, which also ensured good thermal contact with the thermocycler. The entire assembly was covered with a Petri dish cover to prevent ambient perturbations. The CBT shown in Fig. 6(c) was calculated on the phantom data by using the K value from the calibration data. Error shown is taken from using the 95% confidence interval of the K value. Linear fit and R^2 are based on manually set slope of 1 (which assumes constant offset over entire T range). Error bars based on K error propagation (95% confidence intervals), not multiple repeats (n=1 experiment).

Supplementary Information

Information on the polymer synthesis, design and characterization of the readout circuit, and the polymer thermal response and instrument calibration is available in the Supplementary Information.

References

[1] C. A. Paulikas, "Prevention of unplanned perioperative hypothermia," *Aorn Journal*, vol. 88, no. 3, pp. 358–368, 2008.
[2] A. Torossian, "Thermal management during anaesthesia and thermoregulation standards for the prevention of inadvertent perioperative hypothermia," *Best practice & research Clinical anaesthesiology*, vol. 22, no. 4, pp. 659–668, 2008.
[3] S. Moola and C. Lockwood, "Effectiveness of strategies for the management and/or prevention of hypothermia within the adult perioperative environment," *International Journal of Evidence-Based Healthcare*, vol. 9, no. 4, pp. 337–345, 2011.
[4] O. H. Mehta and K. L. Barclay, "Perioperative hypothermia in patients undergoing major colorectal surgery," *ANZ journal of surgery*, vol. 84, no. 7-8, pp. 550–555, 2014.

[5] L. H. Aulick, A. T. McManus, A. D. Mason Jr, and B. A. Pruitt Jr, "Effects of infection on oxygen consumption and core temperature in experimental thermal injury.," *Annals of surgery*, vol. 204, no. 1, p. 48, 1986.

[6] N. M. Bagnall, S. Vig, and P. Trivedi, "Surgical-site infection," *Surgery (Oxford)*, vol. 27, no. 10, pp. 426–430, 2009.

[7] M. J. Kluger, "Body temperature changes during inflammation: their mediation and nutritional significance," *Proceedings of the Nutrition Society*, vol. 48, no. 3, pp. 337–345, 1989.

[8] D. Martelli, S. T. Yao, M. J. McKinley, and R. M. McAllen, "Reflex control of inflammation by sympathetic nerves, not the vagus," *The Journal of physiology*, vol. 592, no. 7, pp. 1677–1686, 2014.

[9] T. Tesch, E. Bannert, J. Kluess, J. Frahm, L. Hüther, S. Kersten, G. Breves, L. Renner, S. Kahlert, H.-J. Rothkötter, *et al.*, "Relationships between body temperatures and inflammation indicators under physiological and pathophysiological conditions in pigs exposed to systemic lipopolysaccharide and dietary deoxynivalenol," *Journal of animal physiology and animal nutrition*, vol. 102, no. 1, pp. 241–251, 2018.

[10] R. Walford, D. Mock, T. MacCallum, and J. Laseter, "Physiologic changes in humans subjected to severe, selective calorie restriction for two years in biosphere 2: health, aging, and toxicological perspectives," *Toxicological Sciences*, vol. 52, no. 2 Supplement, pp. 61–65, 1999.

[11] L. Landsberg, J. Young, W. Leonard, R. Linsenmeier, and F. Turek, "Is obesity associated with lower body temperatures? core temperature: a forgotten variable in energy balance," *Metabolism*, vol. 58, no. 6, pp. 871–876, 2009.

[12] M. D. Coyne, C. M. Kesick, T. J. Doherty, M. A. Kolka, and L. A. Stephenson, "Circadian rhythm changes in core temperature over the menstrual cycle: method for noninvasive monitoring," *American Journal of Physiology-Regulatory, Integrative and Comparative Physiology*, vol. 279, no. 4, pp. R1316–R1320, 2000.

[13] H. Middelkoop, G. Lammers, B. Van Hilten, C. Ruwhof, H. Pijl, and H. Kamphuisen, "Circadian distribution of motor activity and immobility in narcolepsy: Assessment with continuous motor activity monitoring," *Psychophysiology*, vol. 32, no. 3, pp. 286–291, 1995.

[14] M. Van Veen, J. Sandra Kooij, A. Marije Boonstra, M. Gordijn, and E. Van Someren, "Delayed circadian rhythm in adults with attention-deficit/hyperactivity disorder and chronic sleep-onset insomnia," *Biological Psychiatry*, vol. 67, no. 11, pp. 1091–1096, 2010.

[15] M. Bagheri Hosseinabadi, M. Ebrahimi, N. Khanjani, J. Biganeh, S. Mohammadi, and M. Abdolahfard, "The effects of amplitude and stability of circadian rhythm and occupational stress on burnout syndrome and job dissatisfaction among irregular shift working nurses," *Journal of Clinical Nursing*, vol. 28, no. 9-10, pp. 1868–1878, 2019.

[16] D. Weldemichael and G. Grossberg, "Circadian rhythm disturbances in patients with alzheimer's disease: a review," *International Journal of Alzheimer's Disease*, vol. 2010, 2010.

[17] S. Li, Y. Wang, F. Wang, L. Hu, and C. Liu, "A new perspective for parkinson's disease: circadian rhythm," *Neuroscience Bulletin*, vol. 33, pp. 62–72, 2017.

[18] H. Hymczak, A. Gołab, K. Mendrala, D. Plicner, T. Darocha, P. Podsiadło, D. Hudziak, R. Gocoł, and S. Kosiński, "Core temperature measurement—principles of correct measurement, problems, and complications," *International journal of environmental research and public health*, vol. 18, no. 20, p. 10606, 2021.

[19] I. Tsadok, M. Scheinowitz, S. A. Shpitzer, I. Ketko, Y. Epstein, and R. Yanovich, "Assessing rectal temperature with a novel non-invasive sensor," *Journal of Thermal Biology*, vol. 95, p. 102788, 2021.

[20] N. E. Moyen, R. C. Bapat, B. Tan, L. A. Hunt, O. Jay, and T. Mündel, "Accuracy of algorithm to non-invasively predict core body temperature using the kenzen wearable device," *International Journal of Environmental Research and Public Health*, vol. 18, no. 24, p. 13126, 2021.

[21] K.-I. Kitamura, X. Zhu, W. Chen, and T. Nemoto, "Development of a new method for the noninvasive measurement of deep body temperature without a heater," *Medical engineering & physics*, vol. 32, no. 1, pp. 1–6, 2010.

[22] M. Huang, T. Tamura, W. Chen, and S. Kanaya, "Evaluation of structural and thermophysical effects on the measurement accuracy of deep body thermometers based on dual-heat-flux method," *Journal of Thermal Biology*, vol. 47, pp. 26–31, 2015.

[23] M. Huang, T. Tamura, Z. Tang, W. Chen, and S. Kanaya, "A wearable thermometry for core body temperature measurement and its experimental verification," *IEEE journal of biomedical and health informatics*, vol. 21, no. 3, pp. 708–714, 2016.

[24] J. Feng, C. Zhou, C. He, Y. Li, and X. Ye, "Development of an improved wearable device for core body temperature monitoring based on the dual heat flux principle," *Physiological measurement*, vol. 38, no. 4, p. 652, 2017.

[25] J. Fang, C. Zhou, and X. Ye, "Optimization of a wearable device for core body temperature monitoring based on the dual-heat-flux model," in *IOP Conference Series: Materials Science and Engineering*, vol. 677, p. 032006, IOP Publishing, 2019.

[26] K. Tokizawa, T. Shimuta, and H. Tsuchimoto, "Validity of a wearable core temperature estimation system in heat using patch-type sensors on the chest," vol. 108, p. 103294.

[27] N. Panunzio and G. Marrocco, "Flexible and wireless multi-sensor thermometer based on dual-heat-flux model," pp. 29–32.

[28] J. Żmigrodzki, S. Cygan, J. Łusakowski, and P. Lamprecht, "Analytical analysis of factors affecting the accuracy of a dual-heat flux core body temperature sensor," vol. 24, no. 6, p. 1887. Number: 6 Publisher: Multidisciplinary Digital Publishing Institute.

[29] T. H. Kim, Z. Zhou, Y. Choi, V. Costanza, L. Wang, Y. Yun, H. Kang, S. Kim, and C. Daraio, "Flexible biomimetic block copolymer composite for temperature and long-wave infrared sensing," *Science Advances (accepted)*, 2022.

[30] R. Di Giacomo, C. Daraio, and B. Maresca, "Plant nanobionic materials with a giant temperature response mediated by pectin-ca2+," *Proceedings of the National Academy of Sciences*, vol. 112, no. 15, pp. 4541–4545, 2015.

[31] R. Di Giacomo, L. Bonanomi, V. Costanza, B. Maresca, and C. Daraio, "Biomimetic temperature-sensing layer for artificial skins," *Science Robotics*, vol. 2, no. 3, p. eaai9251, 2017.

[32] V. Costanza, L. Bonanomi, G. Moscato, L. Wang, Y. S. Choi, and C. Daraio, "Effect of glycerol on the mechanical and temperature-sensing properties of pectin films," *Applied Physics Letters*, vol. 115, no. 19, p. 193702, 2019.

[33] B. Huber, L. Rossrucker, J. Sundermeyer, and B. Roling, "Ion transport properties of ionic liquid-based polyelectrolytes," *Solid State Ionics*, vol. 247, pp. 15–21, 2013.

[34] J. C. Dyre, P. Maass, B. Roling, and D. L. Sidebottom, "Fundamental questions relating to ion conduction in disordered solids," *Reports on Progress in Physics*, vol. 72, no. 4, p. 046501, 2009.

[35] W. Plazinski and M. Drach, "Binding of bivalent metal cations by α-l-guluronate: insights from the dft-md simulations," *New Journal of Chemistry*, vol. 39, no. 5, pp. 3987–3994, 2015.

[36] U. T. Huynh, A. Lerbret, F. Neiers, O. Chambin, and A. Assifaoui, "Binding of divalent cations to polygalacturonate: A mechanism driven by the hydration water," *The Journal of Physical Chemistry B*, vol. 120, no. 5, pp. 1021–1032, 2016.

[37] L. Wang, T. H. Kim, V. Costanza, N. J. Higdon, and C. Daraio, "Ion transport in thermally responsive pectin film," *Applied Physics Letters*, vol. 123, no. 2, 2023.

[38] Y. Zhang, R. Chad Webb, H. Luo, Y. Xue, J. Kurniawan, N. H. Cho, S. Krishnan, Y. Li, Y. Huang, and J. A. Rogers, "Theoretical and experimental studies of epidermal heat flux sensors for measurements of core body temperature," *Advanced healthcare materials*, vol. 5, no. 1, pp. 119–127, 2016.

[39] N. Mao, M. Song, D. Pan, and S. Deng, "Computational fluid dynamics analysis of convective heat transfer coefficients for a sleeping human body," *Applied Thermal Engineering*, vol. 117, pp. 385–396, 2017.

[40] J. Fitzwater, "A comparison of oral, axillary, and temporal artery temperature measuring devices in adult acute care.," *Medsurg Nursing*, vol. 28, no. 1, 2019.

[41] T. Iden, E.-P. Horn, B. Bein, R. Böhm, J. Beese, and J. Höcker, "Intraoperative temperature monitoring with zero heat flux technology (3m spoton sensor) in comparison with sublingual and nasopharyngeal temperature: an observational study," *European Journal of Anaesthesiology— EJA*, vol. 32, no. 6, pp. 387–391, 2015.

[42] J. Rubia-Rubia, A. Arias, A. Sierra, and A. Aguirre-Jaime, "Measurement of body temperature in adult patients: comparative study of accuracy, reliability and validity of different devices," *International journal of nursing studies*, vol. 48, no. 7, pp. 872–880, 2011.

[43] B. Edwards, J. Waterhouse, T. Reilly, and G. Atkinson, "A comparison of the suitabilities of rectal, gut, and insulated axilla temperatures for measurement of the circadian rhythm of core temperature in field studies," *Chronobiology international*, vol. 19, no. 3, pp. 579–597, 2002.

[44] A. A. Ibrahim, M. Khan, C. Nnaji, and A. S. Koh, "Assessing non-intrusive wearable devices for tracking core body temperature in hot working conditions," *Applied Sciences*, vol. 13, no. 11, p. 6803, 2023.

[45] A. Yoshida, R. Kamon, T. Naka, N. Chigusa, S. Kinoshita, and T. Kawabata, "Evaluation of conventional invasive measurements and examination of non-invasive measurement technique on human body

core temperature," in *IOP Conference Series: Materials Science and Engineering*, vol. 1137, p. 012038, IOP Publishing, 2021.

[46] A. Filippou, I. Louca, and C. Damianou, "Characterization of a fat tissue mimicking material for high intensity focused ultrasound applications," vol. 26, no. 2, pp. 505–515.